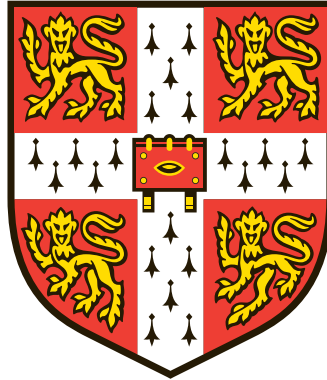


THREE-DIMENSIONAL NANOMAGNETOMETRY: A COMPUTATIONAL STUDY

C. N. Christensen

Hughes Hall



Mini Research Project Report

Centre for Doctoral Training
in Sensor Technologies and Applications

Department of Chemical Engineering & Biotechnology

University of Cambridge

Supervisor: Amalio Fernandez-Pacheco

13 April 2018

**EPSRC Centre for Doctoral Training in
Sensor Technologies & Applications**

The work described in this report is the result of my own research, unaided except as specifically acknowledged in the text, and it does not contain material that has already been used to any substantial extent for a comparable purpose. This report contains 17 pages (excluding this page and the appendices) and ~7000 words.

Signed: _____

Date: _____

(Student)

I confirm that I have cleared the laboratory space I have used for the work described in this report, to the satisfaction of the supervisor of this mini project. All samples have been properly and safely stored or disposed of according to University guidance.

Signed: _____

Date: _____

(Student)

I confirm that the student above has cleared the laboratory space used in this project to my satisfaction.

Signed: _____

Date: _____

(Mini project supervisor)

Three-dimensional nanomagnetometry: a computational study

C. N. Christensen

Hughes Hall

Nanomagnetism is currently a field of great interest for information technology, and a recent trend to bring nanomagnetism into 3D by employing non-planar structures puts a lot of new physics into play and potentially opens the door for novel and revolutionary applications. In order for this transition to 3D structures to happen, reliable measuring methods and computational tools are essential. In this work the magneto-optical Kerr effect (MOKE) is theoretically considered for its potential as the measuring principle of magnetic properties in 3D nanostructures. The first steps towards a framework for computing MOKE in a generalised 3D setting are taken, and schemes to use it for characterisation of geometric and magnetic properties are proposed. Predicted hysteresis loops are compared to experimental results and decent agreement is found.

Preface. The project has been done under supervision of Dr Amalio Fernandez-Pacheco from the Thin Film Magnetism Group at University of Cambridge. Amalio has been very supportive throughout the project, and has insisted on weekly meetings each time providing motivation and interesting new ideas to pursue. Amalio has also put me in contact with PhD students in the group that have been working on topics related to this project, in particular Ddalo Sanz-Hernandez, whom has performed an experiment, elaborated in the following, that has inspired some of the methodology presented in this report.

Contents

1	Introduction	1
2	Magneto-optic Kerr effect	2
2.1	Mistakes in literature	3
2.2	Extension to 3D	4
2.3	Virtual system	5
3	The inverse problems	6
3.1	Inferring the geometry.	6
3.2	Inferring the magnetisation.	6
3.3	Numerical analysis	8
4	Experimental detection schemes	9
5	Hysteresis	9
5.1	Magnetic data and integration	10
5.2	Experimental comparison	10
6	API and GUI	12
7	Outlook	13

8	Conclusion	15
A	Assisting GUI panes	18

1 Introduction

The magneto-optic effects have many useful applications that are studied extensively in the literature. For example imaging of magnetic domains [1] and their propagation in nanostructures, such as ultrathin nanowires using the magneto-optic Kerr effect (henceforth MOKE) [2]. Other applications of the MOKE include measurements of magnetisation responses [3], or surface magnetisation vectors [4], of nanostructures on ultra-fast timescales.

The range of applications underline the technological potential of exploiting the magneto-optic effects.

An exciting trend in recent years, partly driven by recent advances in 3D nanoprinting [5], has been to consider the extension of current magneto-optic applications to three dimensions [5, 6] as envisaged on figure 1. The benefits of extending nanomagnetism into 3D are manifold. It allows for new spin textures with non-trivial topological charges (e.g. vortices and skyrmions) that are far more robust to external perturbations into trivial states [5]. In addition to this enhanced stability, 3D nanomagnets are also expected to have particle-like properties and will yield dramatically higher surface-to-volume ratios relative to planar systems that make them interesting for sensing and actuation applications [5]. Yet another promising possibility of 3D magnets are their use in stor-

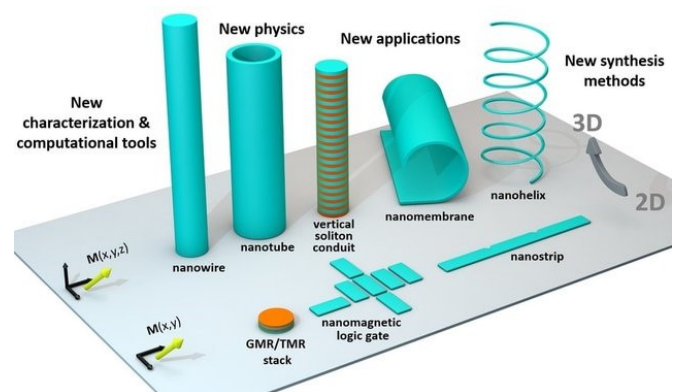


Figure 1: The transition from planar structures to three-dimensional ones gives a lot of liberty to design new applications. New characterisation and computational tools are crucial for this to be realised. Figure from supervisor.

age, where multiple data bits could be stored magnetically in a vertical fashion rather than the planar systems of today, increasing data density significantly and possibly allowing new functionality. Many more possibilities exist, some more exotic such as 3D nanomagnets serving as logic gates opening up new computing architectures [7, 8] or as nodes in magnetic neural networks [9].

Realising applications such as the above-mentioned requires a rigorous theoretical understanding as well as computational capability of the physics in systems with complex 3D geometries. However, the research field of 3D nanomagnets is still only in its infancy, and the literature on computations and characterisations of magnetic 3D nanostructures is very scarce. The main advances have been by experimental studies, of which one will be elaborated in the following, and in particular the MOKE shows promise as the measuring principle for 3D applications. The need for computational methods and the promising experimental advances using MOKE constitute the motivation behind this project. The aim of the project has been to take the first steps towards making a computational framework for simulating the MOKE in a generalised 3D setting and using it for characterisation purposes.

Experimental progress. One of the first reports of successfully using the MOKE for analysis of magnetic nanostructures is a study from 2003 [11], in which a relatively simple optical setup is employed to locate individual magnetic nanowires of down to 100 nm width. The sample considered here does not truly extend into three dimensions as it simply consists of nanowires situated in the surface of a Si substrate, and as such it is difficult to see how their method would generalise to more complex nanostructured geometries, especially those that have unique 3D features extending away from the substrate. The paper ends on the note that their measure-

ments do not reach a limit for the MOKE performance, and encourages others to consider MOKE for the analysis of magnetic nanostructures given that improvements on the sensitivity would be achievable.

Another study [10], primarily by members of the Thin Film Magnetism Group (TFM Group), recently succeeded in fabricating a 3D magnetic conduit and characterised it afterwards using the DF-MOKE method. The nanostructure is a geometry consisting of a 300 nm width ramp, a nanowire, printed on a thin film surface at an angle, such that one end is in direct contact with the surface and the other extends from the surface. The end that touches the surface is called the 2D-3D interconnect, since this is the point at which domain walls can propagate from the thin film substrate into the ramp. The ramp is supported by two non-magnetic pillars to make it more stable. The geometry can be seen on the left of figure 2. Finally a magnetic characterisation is performed using a setup with two opposing detectors and one laser that is positioned at a specific angle matching that of the ramp. The optical setup is shown on the right of figure 2. From this setup the MOKE can be exploited to give distinguishable information about the magnetisation of the film substrate and the ramp. This approach has been dubbed the dark-field MOKE as a reference to the signal reflected from the ramp.

2 Magneto-optic Kerr effect

The MOKE is one of a series of related magneto-optic effects that were discovered in the 19th century. The first of those effects to be discovered is the Faraday effect in an experiment, where Faraday made linearly polarised light propagate through a glass cylinder in a magnetic field parallel to the propagation direction and observed a rotation of the plane of polarisation. Later when the theoretical basis was established by Maxwell it became clear that the phenomenon was well explained by treating

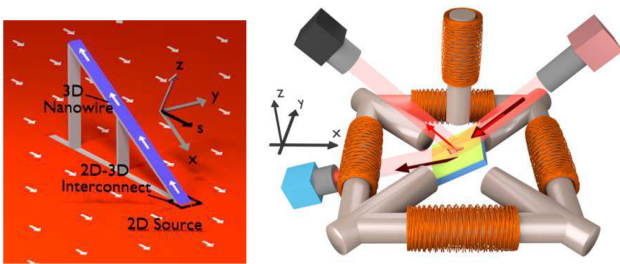


Figure 2: (Left) 3D nanostructure fabricated by printing a nanowire onto a thin film substrate at an angle. Two pillars support the nanowire ramp. (Right) Optical setup used to implement the DF-MOKE method. The blue and red cubes represent the photodetectors, and the black one is the laser, which is angled according to the angle of the ramp of the sample in the center of the diagram. Both images are from [10].

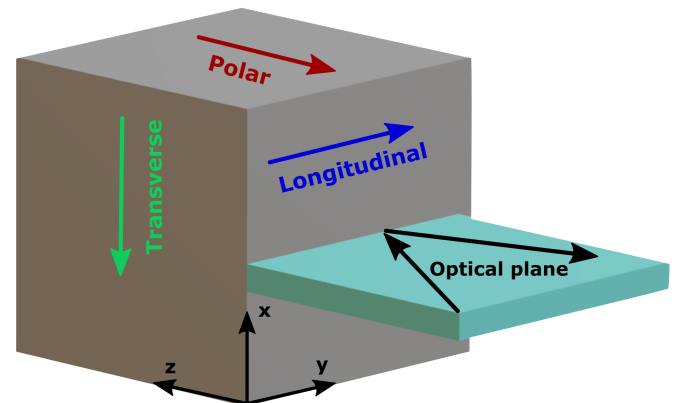


Figure 3: The three special cases of MOKE that are commonly considered: polar, longitudinal and transverse configurations. The shown coordinate system follows that of [16, 17].

the linearly polarised light as a superposition of a left and right circularly polarised beam, which due to circular birefringence travel at slightly different speeds through the medium [12].

A corresponding effect in reflection rather than transmission was discovered by Kerr in 1876, namely the MOKE, i.e. by reflecting light from a magnetised surface a circular birefringence is introduced (or the light may become elliptically polarised if the medium is absorbing, i.e. n is complex, and have elliptical birefringence [13]). Kerr also discovered an electro-optic effect the year prior to this, which is also sometimes referred to as the nonlinear Kerr effect and is the source of nonlinearity in the nonlinear Schrödinger equation [14, 15].

The MOKE is often considered in three special cases referred to as the polar, longitudinal, transverse configurations. As shown on figure 3 these cases correspond to the magnetisation being perpendicular to the surface and parallel to the optical plane (polar), parallel to the surface and optical plane (longitudinal), and parallel to the surface and perpendicular to the optical plane (transverse).

In this report we employ the coordinate system as shown on figure 3. Polarisation states are written using the standard p and s axes, representing the component parallel to the optical plane and the component perpendicular to the optical plane, respectively. The vector $[p \ s]^T$ is referred to as a Jones vector. To describe the rotation of the polarisation state associated with MOKE, we may write the

$$\begin{bmatrix} p_2 \\ s_2 \end{bmatrix}_{\text{reflected}} = \begin{bmatrix} r_{pp} & r_{ps} \\ r_{sp} & r_{ss} \end{bmatrix} \begin{bmatrix} p_1 \\ s_1 \end{bmatrix}_{\text{incident}}, \quad (1)$$

where the polarisation state of the reflected and incident beam is written on the left-hand and right-hand side, respectively. The coefficients of the matrix are referred to as Fresnel reflection coefficients. These coefficients are fairly well documented in the literature. However, in several papers the coefficients appear with small errors, and thus validation of the coefficients is crucial. Details about some of these mistakes will be briefly described in a section below.

Adding to the confusion, some authors do not explicitly state the coordinate system on which their stated coefficients are based on, although it is usually easy to infer the implied coordinate system given familiarity with the MOKE theory and the associated Fresnel coefficients.

The following equations for the coefficients have been compiled after reviewing analytical work by multiple authors to sort out different errors. The generalised Fresnel coefficients of reflection for the Kerr effect are given by [16, 17, 18, 19, 20, 21]

$$r_{pp} = \frac{n_1 \cos \theta_0 - n_0 \cos \theta_1}{n_1 \cos \theta_0 + n_0 \cos \theta_1} - im_x \frac{2n_0 n_1 \cos \theta_0 \sin \theta_1 Q}{(n_1 \cos \theta_0 + n_0 \cos \theta_1)^2}, \quad (2)$$

$$r_{ps} = \frac{in_0 n_1 \cos \theta_0 (m_z \cos \theta_1 - m_y \sin \theta_1) Q}{(n_1 \cos \theta_0 + n_0 \cos \theta_1)(n_0 \cos \theta_0 + n_1 \cos \theta_1) \cos \theta_1}, \quad (3)$$

$$r_{sp} = \frac{in_0 n_1 \cos \theta_0 (m_z \cos \theta_1 + m_y \sin \theta_1) Q}{(n_1 \cos \theta_0 + n_0 \cos \theta_1)(n_0 \cos \theta_0 + n_1 \cos \theta_1) \cos \theta_1}, \quad (4)$$

$$r_{ss} = \frac{n_0 \cos \theta_0 - n_1 \cos \theta_1}{n_0 \cos \theta_0 + n_1 \cos \theta_1}, \quad (5)$$

where θ_0, n_0 and n_1 are the angle of incidence, the refractive index of the nonmagnetic medium, and that of the magnetic medium, respectively. The parameter Q is a constant, referred to as the magneto-optical (MO) constant or Voigt parameter. The variables m_x, m_y and m_z are the components of the magnetisation unit vector.

Thorough derivations of the coefficients can be found in the books by G. S. Krinchik and by K. Zvezdin et al [20].

Validation. The coefficients of (2) through (5) are consistent with the expressions in a recent paper [21], when transforming the coordinate system by $x' = y, y' = -x$ and $z' = z$, where x', y' and z' are the transformed coordinates corresponding to the coordinate system used in the paper. For the special cases, i.e. the polar, longitudinal and transverse cases, the coefficients reduce to simple well-known formulae as seen in [1, 13, 20] assuming appropriate coordinate system transformations.

The implementation of the coefficients has been verified by reproducing certain plots of the coefficients that have been found in the literature [17, 1, 20]. An example is shown on figure 4, in which a coefficient for each of the three different special cases are shown with parameters corresponding to commonly used magnetic compositions; Co/Cu and Co/Pd. The plots that these three reproduce can be found in [20], along with more plots of the other coefficients that have also been reproduced but will be omitted here. The plot for the transverse MOKE special case does not simply show the norm square of a coefficient, but the differential signal $|r_{pp}(Q)|^2 - |r_{pp}(Q=0)|^2$, which corresponds to the signal detected by employing a certain detection scheme.

2.1 Mistakes in literature

In an important work from 1993 [19], the authors Yang and Scheinfein stated the MOKE Fresnel coefficients that they had correctly derived. However, in their formula for r_{pp} , equation (12) in the paper, the Q -dependent term was incorrectly written without a squared denominator. The error was not present later in the same paper, when the coefficients were stated in another context, equation (16), but the typo has prevailed by being reprinted by other authors [16, 17, 20].

In [16] there is a sign error in an expression for the complex Kerr angle, equation (15), and although cor-

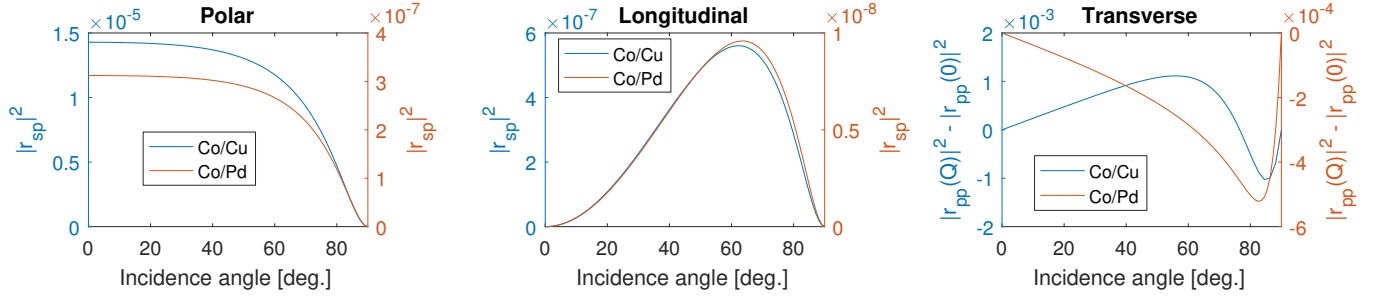


Figure 4: Plots for three special cases of magnetic configuration given two different material compositions: Co/Cu with $n_1 = 1.58 + 3.58i$ and $Q = 0.01772 - 0.0063i$, and Co/Pd with $n_1 = 2.04 + 4.06i$ and $Q = 0.00038 - 0.00314i$. The two leftmost plots show the coefficient $|r_{sp}|^2$, while the rightmost plot shows the differential signal $|r_{pp}(Q)|^2 - |r_{pp}(Q=0)|^2$.

rected in a later paper [17], equation (28), the accompanying text still implies the same error. Another sign error occurs in [16], equation (19), but appears correct in [17].

While some of these errors have brought confusion during the review of the MOKE theory, it has helped to consider several different sources and in particular more recent ones [20, 21].

2.2 Extension to 3D

We shall restrict the treatment of 3D surfaces to convex geometries, i.e. surfaces that do not occlude itself from any angle contrary to concave surfaces. This is a major simplification since we do not need to consider the possibility of multiple reflections from the same object, and the single point of incidence will always be easy to determine. Furthermore, any 3D surface can be thought of as a grid of infinitesimal planes. This is an important realisation, because the problem reduces to computing the MOKE for planar structures situated in 3D space. To image a curved 3D surface, a scanning algorithm that discretises the surface would have to be employed, after which it would be possible to reconstruct the actual curved surface although in an approximative manner depending on the discretisation resolution.

For the previously stated Fresnel coefficients to be applicable in the setting of a 3D plane, we will first define and derive various quantities.

Change of basis. Consider a magnetised plane, representing the sample that is to be measured upon, defined by the normalised normal vector \mathbf{n} and a point in the plane \mathbf{p}_n . Polarised light reflected on this plane will undergo Kerr rotation. To describe polarisation in the ps -basis, we adopt a coordinate system, call it b , with the basis vectors

$$\mathbf{e}_{z'} = \mathbf{k}_1/|\mathbf{k}_1|, \quad \mathbf{e}_{y'} = \mathbf{n} \times \mathbf{e}_{z'}, \quad \mathbf{e}_{x'} = \mathbf{e}_{y'} \times \mathbf{e}_{z'}, \quad (6)$$

where \mathbf{k}_1 is the wave vector of the light.

The basis change matrix ${}_aM_b$ from coordinate system

b to the original, global coordinate system a fulfils

$$\begin{bmatrix} x \\ y \\ z \end{bmatrix}_a = {}_aM_b \begin{bmatrix} x' \\ y' \\ z' \end{bmatrix}_b, \quad (7)$$

where

$${}_aM_b = [\mathbf{e}_{x'} \quad \mathbf{e}_{y'} \quad \mathbf{e}_{z'}]. \quad (8)$$

To transform to b from a the inverse matrix is used

$$\begin{bmatrix} x' \\ y' \\ z' \end{bmatrix}_b = {}_bM_a \begin{bmatrix} x \\ y \\ z \end{bmatrix}_a \quad (9)$$

$$= [\mathbf{e}_{x'} \quad \mathbf{e}_{y'} \quad \mathbf{e}_{z'}]^{-1} \begin{bmatrix} x \\ y \\ z \end{bmatrix}_a. \quad (10)$$

Point of incidence. Given a plane representing the sample with known orientation and position, the point of incidence of a beam travelling towards it will be needed for computations. The point of incidence can be written as

$$\mathbf{h} = \mathbf{p}_0 + s\mathbf{k}_1, \quad (11)$$

where s is found from the orthogonality condition between vectors of a plane and its normal vector

$$\mathbf{n} \cdot (\mathbf{p}_0 + s\mathbf{k}_1 - \mathbf{p}_n) = 0 \Leftrightarrow s = \frac{\mathbf{n} \cdot (\mathbf{p}_n - \mathbf{p}_0)}{\mathbf{n} \cdot \mathbf{k}_1}. \quad (12)$$

Reflection vector. Consider a beam with direction vector \mathbf{k} incident on a plane with normal \mathbf{n} . The direction vector resulting from reflection, referred to as a reflection vector, can be found by using the laws of reflection. In a vector description this means that the reflection vector will have the same inclination to the surface as the incident vector, while it is only the perpendicular component of the incident vector that is reflected. By being reflected the perpendicular component simply changes sign, which

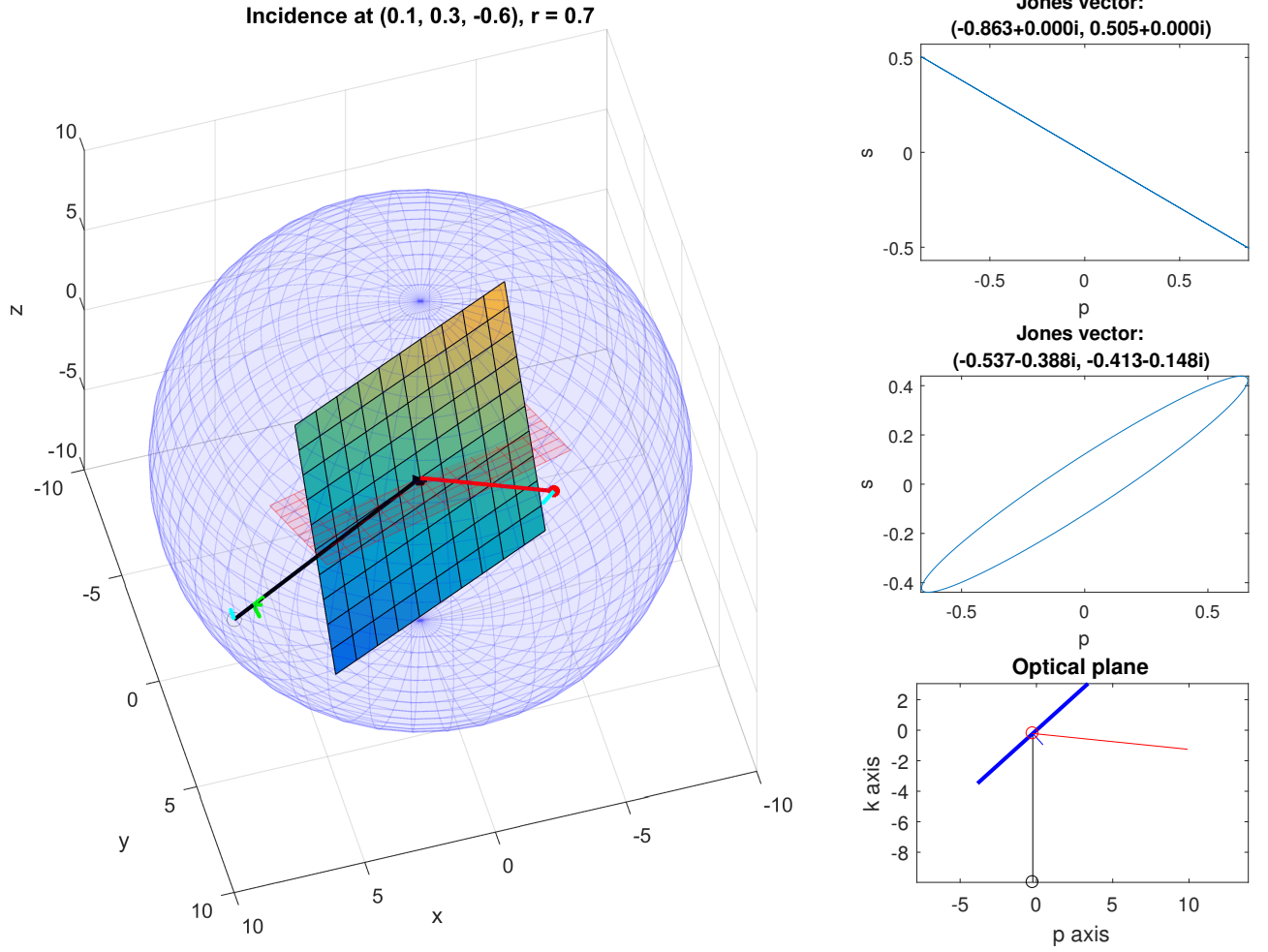


Figure 5: Example of a MOKE computation for the envisaged system of a spherical emitter and detector used in analysis and computations. The black line represents a beam emitted from the shell incident, which is incident on the sample shown as the coloured planar surface. The red line is the reflected beam, which is detected on the shell. The incident beam is chosen to have a random linear polarisation, which is plotted in a sp-plot in the upper-right of the figure with the Jones vector components indicated in the title. The polarisation after reflection is similarly plotted in the middle-right of the figure. In the bottom-right is a 2D projection of the system onto the optical plane, which is performed in the MOKE computation in order to apply the Fresnel coefficients. The randomly generated parameters are: $M = (0.7985, 0.2627, 0.5417)$, $n = (0.3753, 0.7773, 0.5049)$, $p_{\text{start}} = (8.59, 5.11, 0.09)$, $k_1 = (-0.87, -0.49, -0.07)$, where M is the magnetisation, n the sample normal vector, p_{start} is the point on the shell where light is emitted and k_1 is the initial wave vector. The material parameters are those for Co/Cu - $n_1 = 1.58 + 3.58i$ and $Q = 0.01772 - 0.0063i$.

corresponds to removing the component twice from the incident vector,

$$\mathbf{r} = \mathbf{k} - 2\mathbf{n}[\mathbf{k} \cdot \mathbf{n}], \quad (13)$$

where \mathbf{n} is assumed to be a unit vector.

Angle of incidence. A wave vector \mathbf{k}_1 directed at a plane with normal \mathbf{n} , both vectors assumed to be normalised, has an angle of incidence given by

$$v = \min[\text{acos}(\mathbf{k}_1 \cdot \mathbf{n}), \pi - \text{acos}(\mathbf{k}_1 \cdot \mathbf{n})], \quad (14)$$

where the min function ensures that the angle is almost at most 90 degrees, even when the normal vector is not directed towards the incident beam.

2.3 Virtual system

To make analysis and computations in the following sections more concrete, we shall consider a specific system without loss of generality. This system consists of a spherical detector and emitter with a sample somewhere inside it. This means that light can be emitted in any direction towards the interior of the sphere from any position on the shell, and regardless of the position and orientation of the sample, the reflected beam will propagate back to

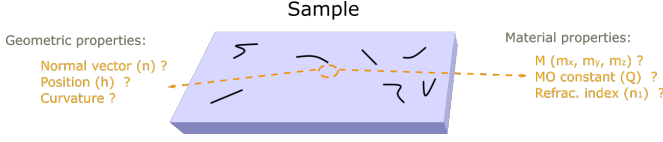


Figure 6: Unknown parameters that are addressed in the inverse problems. Inferring the geometric and material properties are treated as two separate problems.

the shell and be detected.

The system is shown on figure 5, where a random instance is used as an example. For an incident beam with linear polarisation state, shown as the black line, the MOKE is seen to induce ellipticity in the reflected polarisation state due to circular birefringence imposed by the imaginary part of the used MO constant Q .

3 The inverse problems

We shall now consider the problem of characterising a sample of which nothings is known – see figure 6. There are both geometric parameters and material parameters (most importantly, the magnetisation and MO constant), and there will be a distinction of the problems of characterising each type of parameters. We seek to infer the parameters from performing measurements of reflection and MOKE, and therefore the problems will be referred to as the inverse problems, or the inverse geometry and inverse magnetisation problem, respectively.

3.1 Inferring the geometry.

The geometry refers to the orientation and position of a planar sample in space. To infer this by measurements of reflection, a scheme will be employed that uses two beams with wave vectors \mathbf{k}_i , source points \mathbf{p}_i and destination points \mathbf{q}_i ; source and destination points meaning point of emission and detection, respectively. The key point of the scheme to obtain a fully determined solvable problem is

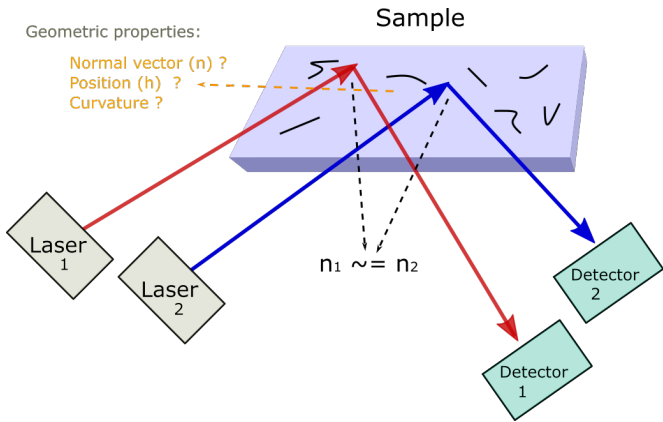


Figure 7: Overview of the scheme for the inverse geometry problem showing the unknown parameters to be determined: plane orientation and position.

to prepare the two beams that are linearly independent, i.e. with either different source points or different initial wave vectors. The scheme is shown on figure 7. Let each beam be incident on the plane at position \mathbf{h}_i . The equations that each beam provides are then given by the two coupled nonlinear equations

$$\mathbf{p}_i + \sqrt{(\mathbf{h}_i - \mathbf{p}_i)^2} \mathbf{k}_i = \mathbf{h}_i, \quad (15)$$

$$\mathbf{h}_i + \sqrt{(\mathbf{q}_i - \mathbf{h}_i)^2} (\mathbf{k}_i - 2\mathbf{n} [\mathbf{k}_i \cdot \mathbf{n}]) = \mathbf{q}_i. \quad (16)$$

The equations simply describe the relation between the source, incidence and destination points based on the wave vector, normal vector and reflection vector. As the vectors are three-dimensional, each beam provides 5 linearly independent equations and introduces 3 unknowns, and along with the normal vector of the plane, there is collectively 10 linearly independent equations and 9 unknowns when using the two beams. Had there only been a single beam, the problem would be underdetermined, since there would then be 6 unknowns and 5 linearly independent equations. A closed-form solution does not exist due to the nonlinearity, but a nonlinear least squares numerical method can be employed to solve

$$(\mathbf{n}, \mathbf{h}_1, \mathbf{h}_2) = \arg \min_{\mathbf{n}, \mathbf{h}_1, \mathbf{h}_2} \sum_{i=1,2} \left[\left(\frac{\mathbf{h}_i - \mathbf{p}_i}{\sqrt{(\mathbf{h}_i - \mathbf{p}_i)^2}} - \mathbf{k}_i \right)^2 + \left(\frac{\mathbf{q}_i - \mathbf{h}_i}{\sqrt{(\mathbf{q}_i - \mathbf{h}_i)^2}} - \mathbf{k}_i + 2\mathbf{n} [\mathbf{k}_i \cdot \mathbf{n}] \right)^2 \right] \quad (17)$$

3.2 Inferring the magnetisation.

In this problem the magnetisation, the MO constant and the refractive index of the sample are desired quantities. We assume that the inverse geometry problem has been solved, such that the sample plane's normal is known.

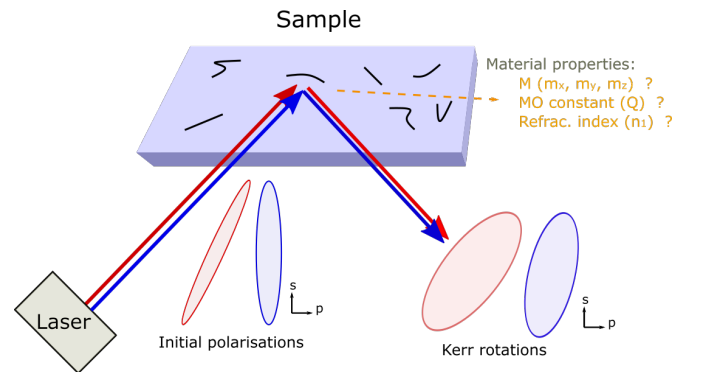


Figure 8: Overview of the scheme for the inverse magnetisation problem showing the unknown parameters to be determined: magnetisation vector, MO constant and refractive index.

For this scheme consider two separate measurements of the Kerr rotation of a light beam prepared to have different polarisation states but the same wave vector \mathbf{k}_1 in the two measurements – see figure 8. Let the initial Jones vector in each measurement be $\mathbf{J}_1 = (p_1, s_1)$ and $\mathbf{J}_2 = (p_2, s_2)$. The resulting Jones vector after Kerr rotation of \mathbf{J}_i is given by

$$\mathbf{J}_i' = G\mathbf{J}_i \Leftrightarrow \begin{bmatrix} p_i' \\ s_i' \end{bmatrix} = \begin{bmatrix} r_{pp} & r_{ps} \\ r_{sp} & r_{ss} \end{bmatrix} \begin{bmatrix} p_i \\ s_i \end{bmatrix}, \quad (18)$$

where G is the matrix of Fresnel reflection coefficients related to the magneto-optic Kerr effect. The formulae for these coefficients are known analytically, (2) through (5), but in the case of the inverse problem, these formulae cannot be evaluated as they depend on the unknowns. Instead we determine the coefficients based on the two polarisation measurements

$$\begin{bmatrix} p_1' \\ s_1' \\ p_2' \\ s_2' \end{bmatrix} = \begin{bmatrix} p_1 & s_1 & 0 & 0 \\ 0 & 0 & p_1 & s_1 \\ p_2 & s_2 & 0 & 0 \\ 0 & 0 & p_2 & s_2 \end{bmatrix} \begin{bmatrix} r_{pp} \\ r_{ps} \\ r_{sp} \\ r_{ss} \end{bmatrix} \quad (19)$$

$$\Leftrightarrow \begin{bmatrix} r_{pp} \\ r_{ps} \\ r_{sp} \\ r_{ss} \end{bmatrix} = \begin{bmatrix} p_1 & s_1 & 0 & 0 \\ 0 & 0 & p_1 & s_1 \\ p_2 & s_2 & 0 & 0 \\ 0 & 0 & p_2 & s_2 \end{bmatrix}^{-1} \begin{bmatrix} p_1' \\ s_1' \\ p_2' \\ s_2' \end{bmatrix} \quad (20)$$

We shall now distinguish between the analytically determined coefficients from equations (2)-(5) and the ones inferred from measurements in (20). Let the former be denoted as functions of the unknowns $r_{ij}(Q, m_x, m_y, m_z)$ and the latter as constants r_{ij}^* . The coefficient r_{ss} does not depend on the magnetisation as seen in (5), and so the measured quantity r_{ss}^* can be used outright to determine n_1 from the coefficient formula and Snell's law $n_0 \sin \theta_0 = n_1 \sin \theta_1$, and upon simplifying the expression, one ends up with

$$n_1 = \frac{n_0 \sqrt{1 - 2r_{ss}^* \cos(2\theta_0) + (r_{ss}^*)^2}}{\sqrt{(r_{ss}^* + 1)^2}}. \quad (21)$$

The denominator cannot be reduced further, because r_{ss}^* is complex in general. Note that (21) may yield a value of n_1 with an incorrect sign, but it is easy to compensate for this by checking whether the real part of n_1 is positive (as it physically has to be), and inverting the sign if this is not the case.

The other unknowns may now be found by solving the nonlinear set of equations

$$r_{ij}(Q, m_x, m_y, m_z) = r_{ij}^* \quad | \quad i, j \in \{s, p\}, \quad (22)$$

with the constraint that $\sqrt{m_x^2 + m_y^2 + m_z^2} = 1$, because the magnetisation vector is a unit vector by definition. The square root is included to make it clear that it is a constraint on the norm, although it could be omitted.

Again there are no closed-form solution due to nonlinearity, but a nonlinear least squares method can be used to solve

$$(Q, m_x, m_y, m_z) = \arg \min_{Q, m_x, m_y, m_z} \sum_{i,j \in \{s,p\}} \left[\left(r_{ij}^* - r_{ij}(Q, m_x, m_y, m_z) \right)^2 + \left(\sqrt{m_x^2 + m_y^2 + m_z^2} - 1 \right)^2 \right]. \quad (23)$$

Furthermore, the method should be implemented such that only Q is assumed to be complex, while (m_x, m_y, m_z) is a real vector. Alternatively, one could replace the last term in the objective function, $\left(\sqrt{m_x^2 + m_y^2 + m_z^2} - 1 \right)^2$, with the two terms $\left(\sqrt{\text{Re}(m_x)^2 + \text{Re}(m_y)^2 + \text{Re}(m_z)^2} - 1 \right)^2 + \left(\text{Im}(m_x)^2 + \text{Im}(m_y)^2 + \text{Im}(m_z)^2 \right)$, because when each of these terms are minimised the norm of the real part will be 1 and the norm of the imaginary part will be 0.

The combined inverse problem. The two inverse problems have now been treated individually, although the inverse magnetisation problem relied on the inverse geometry problem being solved first. A measurement in the inverse geometry problem will be referred to as a triangulation measurement, because it is related to the angle of reflections. For the complete inverse problem of first inferring the geometry and point of incidence followed by a determination of the magnetisation, one would need two triangulation measurements for the geometry, as we have seen, and then measure the final polarisation of two beams with equal wave vectors but different initial polarisation states – thus, a total of four measurements. If the polarisation was also to be measured in the triangulation part, one of these measurements could be reused in the magnetisation determination, such that only one new measurement is needed. In this scheme a total of three measurements are required. However, an approximation can be employed in which both triangulation measurements are reused in the determination of the magnetisation. The premise of this approximation is that if the points of incidence of the two triangulation beams are close enough in space, then the magnetisation vectors at those two positions will not differ significantly and it is justified to treat them as the same. Hence, depending on how small changes to the wave vector can be made while still being significantly distinguishable for the triangulation (i.e. depending on the measurement precision and associated noise), the scheme can be made to only use two measurements in total (of final beam position and polarisation) to determine point of incidence at the sample, its normal and its magnetisation.

The nonlinear least squares method. There are multiple possible methods for solving the two nonlinear

least squares problems. Those employed by MATLAB by default is the quasi-Newton trust-region method (referred to as trust-region-reflective) and Levenberg-Marquardt algorithm. The trust region method has the advantage of handling bounds, which is helpful since each inverse problem involves a unit vector: the normal vector and the magnetisation vector, respectively. Thus in solving for these quantities we can configure the method to not look for components that are below -1 or above 1. The two aforementioned algorithms are both Newton step-based methods, meaning that they approximate the objective function by its linearisation based on the Jacobian (first-order) or potentially the Hessian (second-order) [22]. That is, for an objective function f that depends on the parameter vector x , the linearisation $f(x + \delta x) \approx f(x) + J\delta x$ is used, where J is an estimate of the Jacobian of the objective function. How well this approximation works, which is to say how quickly the method converge overall, depends wholly on the objective function as we shall see in the next section.

3.3 Numerical analysis

A numerical method is said to be consistent if it has an order p greater than 0 such that the local truncation error of the n th step is bounded by $\delta_n^h = O(h^{p+1})$, where h is a discretisation parameter, e.g. step size [23]. Consistency and stability are the two necessary and sufficient conditions for convergence. Stability analysis is out of the scope of this work, but the numerical methods suggested in previous section will now be investigated for consistency and convergence with stability being assumed.

Rather than considering the step size used internally in the numerical methods, we shall for simplicity consider the local truncation error as a function of iteration count. The iteration count of a method is not in general proportional to the step size, but for a consistent method the step size should monotonically decrease as the iterations progresses, which is sufficient to show that $p > 0$.

Figure 9 shows the norm of the objective function that is minimised (referred to as the error norm) versus the relative iteration count for executions of the inverse problem's respective method. The plot uses a relative iteration count on the first axes rather than the absolute iteration count, because the latter is hugely different between the two methods. The method treating the geometrical inverse problem only 15 iterations to reach the desired tolerance, whereas inferring the magnetisation requires as much as 236 iterations. This is clearly seen in the density of data points on each curve.

The absolute iteration count depends on the quality of the initial guess provided to the solver – i.e. the starting point of the solver, which is randomly generated in the implementation, but could potentially be replaced with a qualified guess if some heuristic was found. Hence, to demonstrate convergence in a more general sense, the solution process should be repeated for many different

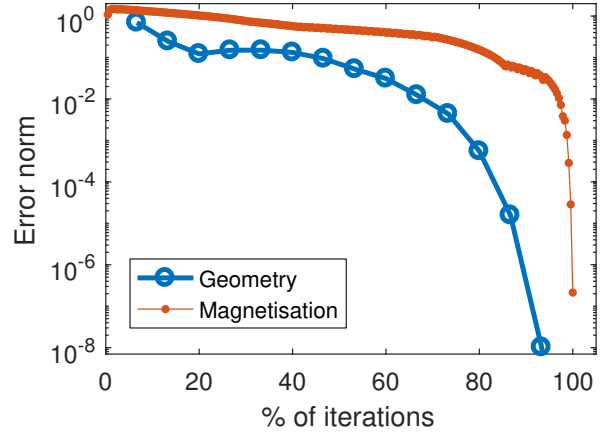


Figure 9: Convergence plots of the two nonlinear least squares methods for the two respective problems of inferring geometry and magnetisation. For the inverse geometry problem the *unknown* plane (used to perform a virtual measurement, which is then used to compute "backwards") is defined from the normal $n = -(1, 3, 1)$ and the point in the plane $p_n = (4, 3, 3)$, while the two wave vectors are $k_1 = (1, 1, 1)$ and $k_2 = (1.5, 1, 1)$. For the inverse magnetisation problem the parameters used are $n = (-0.3015, -0.9045, -0.3015)$, $M = (0.8503, -0.0923, -0.5181)$, $Q = 0.0177 - 0.0063i$. Iteration count is 15 and 236 respectively for the same objective function tolerance of $1e-14$.

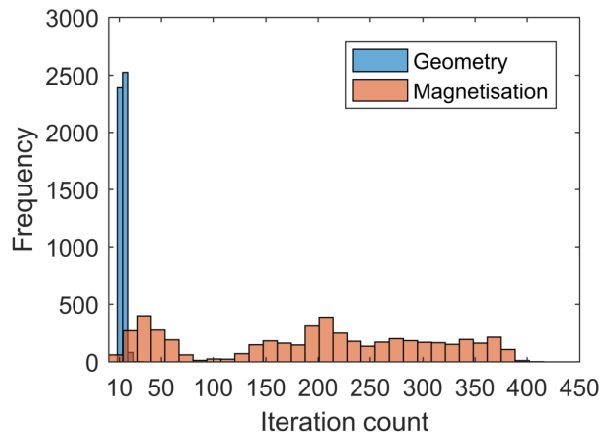


Figure 10: Histogram of iterations counts for 5000 executions of the nonlinear least squares methods for the two respective problems of inferring geometry and magnetisation. For each execution the starting guess is randomly generated to get a better idea of the general performance of the method for each problem. Parameters used are as denoted in 9.

random starting guesses. This has been done with 5000 repetitions of each inverse problem's method, and the resulting histogram of iteration counts can be seen in figure 10.

The maximum allowed number of iterations was set to 800, but none of the instances required near as many,

meaning that all instances converged to the specified objective function tolerance of $1e-14$. As was also indicated by figure 9, the histograms make it very clear that the inverse geometry problem is significantly easier to solve than the inverse magnetisation problem. The reason for this is simply that the objective function of the inverse magnetisation problem is less prone to linearisation. As mentioned in the end of last section, the nonlinear least squares method uses a Newton step-based approximation to linearise the objective function. Considering the objective function of the inverse geometry problem, eq. (17), it seems clear that it is more suited for linearisation given that the expression consists of vector product and vector normalisations. On the other hand the objective function of the inverse magnetisation problem, eq. (23), is more convoluted due to the intricate formulae for the MOKE coefficients, eq. (2) through (5), causing the objective function to only be crudely approximated by linearisation, thus requiring more iterations in total for the method to converge.

4 Experimental detection schemes

In the previous section it has implicitly been assumed that one can measure the real and imaginary components of the polarisation state. This is not directly possible since detectors by default measures intensity, and thus only the norm square is obtained. There are several ways in which the ellipticity of the polarisation state (the complex nature) can be addressed however, and in this section we shall consider some optical components that can help to that end.

Passive optical components can be described with Jones calculus. For the detection schemes considered in the following, we will be needing to describe an arbitrary angle polariser, or analyser, a polarisation rotator, circular polarisers and a generalised wave plate. In respective order these are given by [12]

$$T_{\text{pol}}(v) = \begin{bmatrix} \cos^2(v) & \cos(v)\sin(v) \\ \cos(v)\sin(v) & \sin^2(v) \end{bmatrix}, \quad (24)$$

$$T_{\text{rot}}(v) = \begin{bmatrix} \cos(v) & -\sin(v) \\ \sin(v) & \cos(v) \end{bmatrix}, \quad (25)$$

$$T_{\text{circ,right/left}}(v) = \frac{1}{2} \begin{bmatrix} 1 & \pm i \\ \mp i & 1 \end{bmatrix}, \quad (26)$$

where the signs in $T_{\text{circ,right/left}}$ should be read from top to bottom depending on whether a right or left circular polariser is desired. Finally, for the generalised wave plate [24]

$$T_{\text{waveplate}}(v, \eta) = e^{\frac{i\eta}{2}} \begin{bmatrix} \cos^2(v) + e^{-i\eta} \sin^2(v) & (1 - e^{-i\eta}) \sin(v) \cos(v) \\ (1 - e^{-i\eta}) \sin(v) \cos(v) & \sin^2(v) + e^{-i\eta} \cos^2(v) \end{bmatrix}, \quad (27)$$

where the angle v is the orientation of the fast axis with respect to the p -axis and η is birefringence, i.e. the phase

retardation induced between the fast and slow axis, $\eta = \phi_s - \phi_p$, which is $\pm\pi$ for a half-wave plate and $\pm\pi/2$ for a quarter-wave plate.

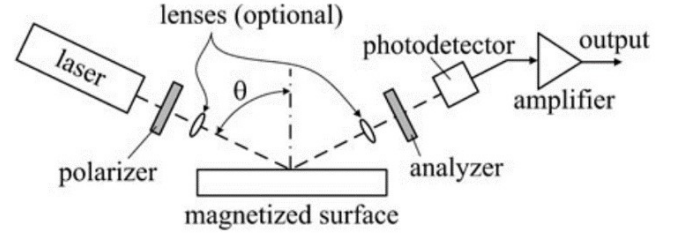


Figure 11: Direct detection scheme used in this work, although the polariser and analyser may be replaced by other components as specified. Figure from [20].

For the remainder of this report the detection scheme illustrated on figure 11 will be assumed, where the stage before and after reflection will be allowed to consist of any combination of the components described above. The amplifier will not be relevant, since noise sources are not being modelled and absolute values of the intensities are troublesome, as argued in the next section. Thus, the signal from the photodetector will simply be the norm square of the polarisation state, $|J_p|^2 + |J_s|^2$, in arbitrary units.

5 Hysteresis

Ferromagnetic like paramagnetic materials can be magnetised, but ferromagnetic materials have the property that they retain the magnetisation applied by an external field. This effect of magnetic memory is the cornerstone in many magnetic applications, e.g. hard drives, and is referred to as hysteresis¹. In characterising a ferromagnetic material the hysteresis behaviour is often of interest, which can be quantified via a hysteresis loop. The loop is generated by observing the magnetisation while linearly varying the external field through a range of values and back again to its starting point.

Since MOKE depends heavily on magnetisation, it is no surprise that hysteresis will be clearly present in a MOKE signal during the sweep of the external field. However, the MOKE coefficients as seen in section 2 do not have a proportional dependence on the respective magnetisation components. Hence, while generating a hysteresis loop the obtained MOKE signal will in general be a superposition of the hysteresis loop along each component. For that reason a symmetrical magnetic hysteresis may exhibit an asymmetrical MOKE signal.

In this section we shall consider how to simulate such MOKE signals given that the hysteresis behaviour of the magnetic sample is known. The virtual system employed

¹However, note that hysteresis is not exclusive to ferromagnetic ordering – another example being spin glass ordering [25]

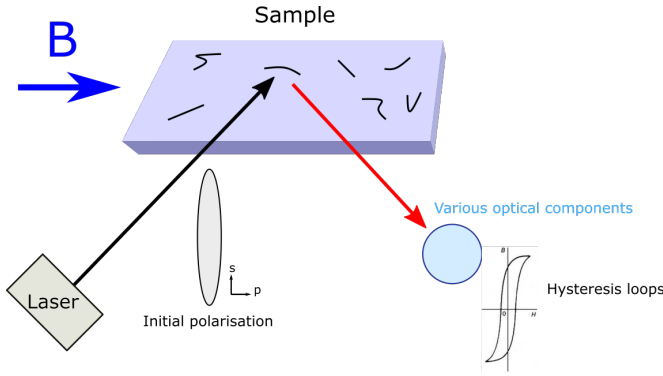


Figure 12: Optical setup to quantify hysteresis loops via MOKE. The optical components represent different detection schemes.

is that indicated by 12, in which the external field B is varied and the optical signal resulting from a particular detection scheme is continuously measured. The initial polarisation emitted by the laser can be anything, but is naturally kept constant through the sweep of the external field.

5.1 Magnetic data and integration

To simulate a MOKE hysteresis loop it is required that the magnetic sample's response to the external field is known. For a certain material composition the information could possibly be obtained experimentally, but alternatively a software package such MuMax [26] can be used to simulate the material and obtain a numerical approximation of its hysteresis behaviour.

In the following we shall consider such magnetic simulation data provided by the TFM Group. The data consists of a sequence of three-dimensional arrays; each array corresponding to one value of the external magnetic field, and each data point in the arrays corresponding to one coordinate in a 3D grid representing the material's spatial distribution.

This will be used to compute the MOKE signal that can then be compared to an experiment performed by the TFM Group.

The distribution of magnetisation may not be uniform, in which case the beam profile might have to be considered for an accurate description. Additionally, the material may not be perfectly reflective, and the penetration depth into the material would have to be accounted for. Allowing the beam to penetrate the surface also opens the possibility of interferometric effects inside the material, but this will be neglected straight away. Penetration into materials is typically modelled with the Beer-Lambert law, which states that the intensity decays exponentially according to $I(z) = I_0 \exp(-z/z_0)$, where I_0 is the intensity at the surface, z is the depth and z_0 is the characteristic penetration depth [27].

If the spatial beam width is smaller than the length

scale of the sample, a volume integral weighted by beam intensity could be evaluated to obtain a weighted average of the magnetisation at the point of incidence of the beam's centre, which would be used for the MOKE computation. On the other hand if the spatial beam width is much larger than the length scale of the sample, then the effective magnetisation simply becomes the average magnetisation along each component (along each axis), because the weighted average effectively has a constant weight function.

In general the weighted average of magnetisation at a point $p = (x', y', z')$ would be

$$\bar{M}(p) = \iiint_V M(x, y, z) W(p, x, y) e^{-z/z_0} dS, \quad (28)$$

where the volume V represents the sample and $W(p, x, y)$ is the weighting function. The weight function, e.g. a two-dimensional Gaussian distribution given a Gaussian beam profile, in which case the centre of the distribution would be the point p . The formulae (28) assumes that the sample is aligned with the xy -plane, otherwise a coordinate system transformation would have to be used.

However, while accounting for beam profile and collimation rather than considering beams may be more accurate, it also adds another layer of complexity to the computations. Thus, to start with we shall consider that $W(p, x, y, z) = 1$. Furthermore, as another simplification that could later be undone, we shall assume that the sample is planar, which makes the surface integral easier. Given a distribution of magnetisation discretised into a $N \times N$ grid, the effective magnetisation is

$$\bar{M} = \frac{1}{N^2} \sum_{r=1}^N \sum_{c=1}^N M(r, c). \quad (29)$$

The MuMax simulation results provided by the TFM Group are shown in one instant during the variation of the external field B in figure 13. The corresponding value of B is 10 mT along the y -axis, which is a relatively small magnitude since the complete range covers -300 to 300 mT. For the extreme values in this range, the magnetisation is essentially parallel to the plane in the respective directions.

A surface integration of this distribution as a function of the external field magnitude provides the hysteresis loops along each component shown in figure 14. As seen the hysteresis loop along the x -component is essentially zero, while in the other two components there is a significant hysteresis of symmetrical and anti-symmetrical nature.

5.2 Experimental comparison

Having now the magnetic configuration from MuMax with a way to compute effective magnetisation, and the ability to implement various detection schemes with optical components described via Jones calculus, it is time

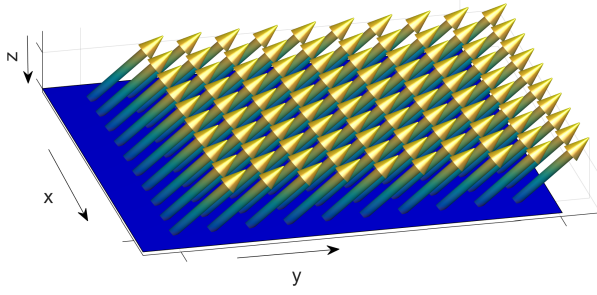


Figure 13: Snapshot of the magnetic distribution during the variation of the external field B .

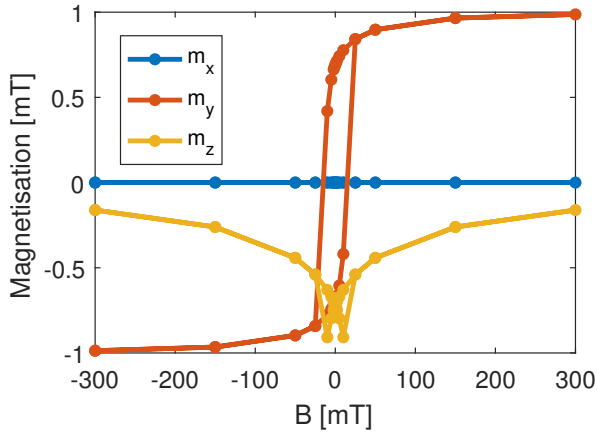


Figure 14: Hysteresis loops provided by a magnetic simulation in the software MuMax.

to consider results and compare them with corresponding experimental results provided by the supervisor of this project, whom has fabricated the sample and performed the measurements. The material investigated is a multilayer Co/CoFeB structure described further in [28]. The physical parameters used in computations however will be those of Co/Cu - $n_1 = 1.58 + 3.58i$ and $Q = 0.01772 - 0.0063i$. The angle of incidence in the experiment was estimated to be 30 degrees.

The complex Kerr angle ϕ_k with Kerr rotation θ_k and ellipticity ϵ_k is defined as [1]

$$\phi_{k,s} = \theta_{k,s} + i\epsilon_{k,s} = \frac{r_{ps}}{r_{ss}} \quad \text{and} \quad \phi_{k,p} = \theta_{k,p} + i\epsilon_{k,p} = \frac{r_{sp}}{r_{pp}}. \quad (30)$$

The coefficient r_{ss} does not depend on magnetisation, and r_{pp} only depends on the magnetisation for the transverse MOKE, which is generally much weaker experimentally. Hence, the coefficients r_{pp} and r_{ss} are essentially expected to both be constant when varying the external field, such that only the coefficients r_{ps} and r_{sp} are important for the change in polarisation as a function of magnetisation.

The MOKE signal will in general be a linear combination of the coefficients and the polarisation before reflection. While it will not be possible to measure upon

the two variants of the complex Kerr angle given by (30) directly, as the signal will be a mixture of the coefficients, the Kerr rotation and ellipticity will still be addressed, respectively, i.e. the real and imaginary parts of the mixed rotation.

For the virtual measurements it is assumed that the initial polarisation is at a plus or minus 45 degree angle in the ps -plane. A sign change of the polarisation angle will just mirror the resulting signal in an axis, and will not change the qualitative variation.

For a measurement of the Kerr ellipticity a quarter wave plate is needed to make the incident polarisation complex, causing the polarisation change of the imaginary part to be more significant in the measured signal. The resulting signal versus the experimentally obtained signal is shown in figure 15. The scaling on the secondary axis is arbitrary, because it depends on many unknown parameters in the experimental setup - not only may there be multiple sources of loss during propagation and imperfect alignment, but the exact operation of the detector (as in internal resistance etc.) would have to be understood.

Clearly there is a qualitative agreement between the curves; the asymptotes have similar slope and the asymptotic flatness roughly coincides between -50 and 0 mT in case of the negative asymptote, although the positive asymptote is a bit off as the flatness also occurs between -50 and 0 mT for the experimental signal, whereas the numerical signal is complete symmetrical and starts being visibly flat between 0 and 50 mT. This bias between the signals is not unexpected and will be addressed later in this section.

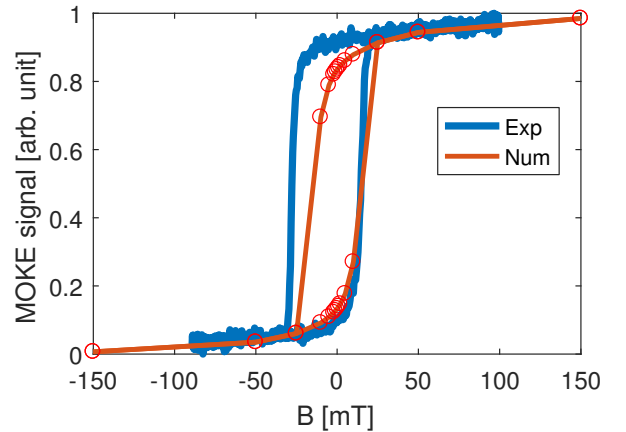


Figure 15: Comparison with experimental ellipticity measurement. The corresponding optical setup consists of a quarter wave plate with a 90 degree angle of the fast axis w.r.t. the p axis, and an analyser at 45 degrees with the p axis.

To measure the Kerr rotation only an analyser at 0 degrees after reflection is needed. The resulting signal versus the experimentally obtained signal is shown in figure

16. Again, there is a reasonable qualitative agreement. The slope of the right tail seem a bit off, but the same kind of asymmetry is present in both signals. This asymmetry is due to the above-mentioned mixture of coefficients, which effectively results in a linear combination of the hysteresis loops shown in figure 14 – additively combining a fraction of the antisymmetric m_y signal with the symmetric m_z signal yields an asymmetric signal.

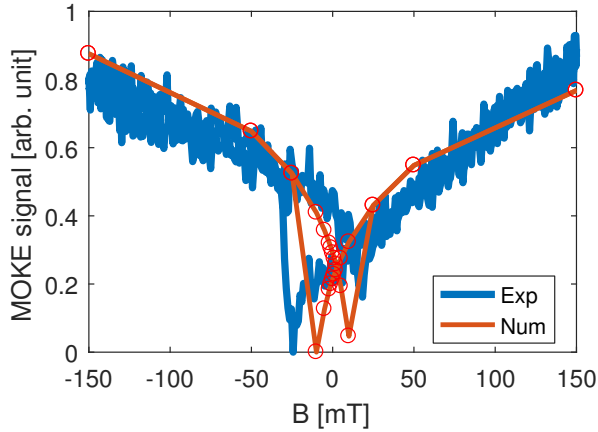


Figure 16: Comparison with experimental rotation measurement. The corresponding optical setup consists only of an analyser at 0 degrees with the p axis.

However, there is also a clear bias again; a shift of the experimental signal towards the left. The bias in both cases is presumed to be due to noncollinear quantum exchange interaction known as Dzyaloshinskii-Moriya interaction as described in [29, 30]. This type of interaction is known to be able to cause a phenomenon called exchange bias [31], in which a ferromagnetic film can have its magnetisation curve shifted due to the presence of layers with other ordering.

6 API and GUI

One of the end goals of the computational study of this project has been to wrap the implementations into an API (application programming interface) to be used for MOKE computations by others, in particular those of the TFM Group. The main use case is to be able to probe a magnetic sample of known magnetisation (for instance the data obtained from a MuMax simulation) in order to generate a prediction of the associated MOKE signal under various optical conditions that the user can specify.

A front-end to the API has also been desired to make it more quick and accessible to use. The GUI (graphical user interface) presents the results, but also allows parsing and specification of the data and parameters stated above. The GUI can be seen in figure 17.

Magnetisation data. The parsing of the magnetisation data is specified through the textfield in the upper

left, where a path of a MuMax folder or a textfile (un-compressed data file) is put.

If the path of a MuMax folder is provided, a sequence of files is expected. Each file must correspond to a certain value of the external field and have a filename according to $*_{*}.*.ovf$ – the first wild star character can be anything, but the second should contain a number representing the external field magnitude, e.g. $*_{150}mT.ovf$. The $.ovf$ file extension is the default type used by MuMax. Upon pressing load all the $.ovf$ files will be processed, and the summation corresponding to a planar surface integration with constant weight function, eq. (29), is performed by the program. The magnetisation averages appears in the three right-most columns underneath the path textfield in the GUI, while the leftmost of the four columns shows the magnitude of the external field derived from the filenames. The values of the magnetic component averages are then plotted against the external field magnitude and shown in the three plots in the bottom-left of the GUI – these graphs are similar to those shown previously in figure 14 (note that the plot for \bar{m}_x , titled B vs M_x , has an axis scaled by 10^{-11} and is therefore still essentially zero).

The other way to parse magnetisation data via the textfile assumes that the magnetisation component averages have been precomputed and are given directly in a table following a delimiter-separated textfile specifying with each row specifying a magnitude of the external magnetic field and then the three component averages \bar{m}_x , \bar{m}_y and \bar{m}_z . The provided file can be with extension $.txt$, $.csv$ or $.dat$, and it may use any standard type of delimiter and have any number of header lines.

Finally, the aforementioned four columns are editable and so the component averages can also manually be provided by typing or copy-pasting into these textfields. After values have been provided this way, the update button in the lower left must be pressed to have the data plotted in the bottom three figures.

Physical parameters. Before computations can be performed, the rubric with "Physical parameters" must be filled. The two refractive indices must be provided, and the MO constant, Q , and finally the incidence angle Θ in degrees. There are also three standard material compositions that can be chosen causing the fields to be auto-filled with corresponding values, namely Co/Cu, Co/Pd and permalloy.

If the user wishes to do the simulation in a 3D setting, according to the computations of section 2.2, the two fields in the bottom of the rubric can be filled, i.e. the normal vector of the sample n and the incident wave vector k . Those values will overrule whatever is specified in the field for Θ . The angle of incident implied by the normal vector and wave vector will be output to the user in the output field in the lower-right of the GUI once a computation is performed.

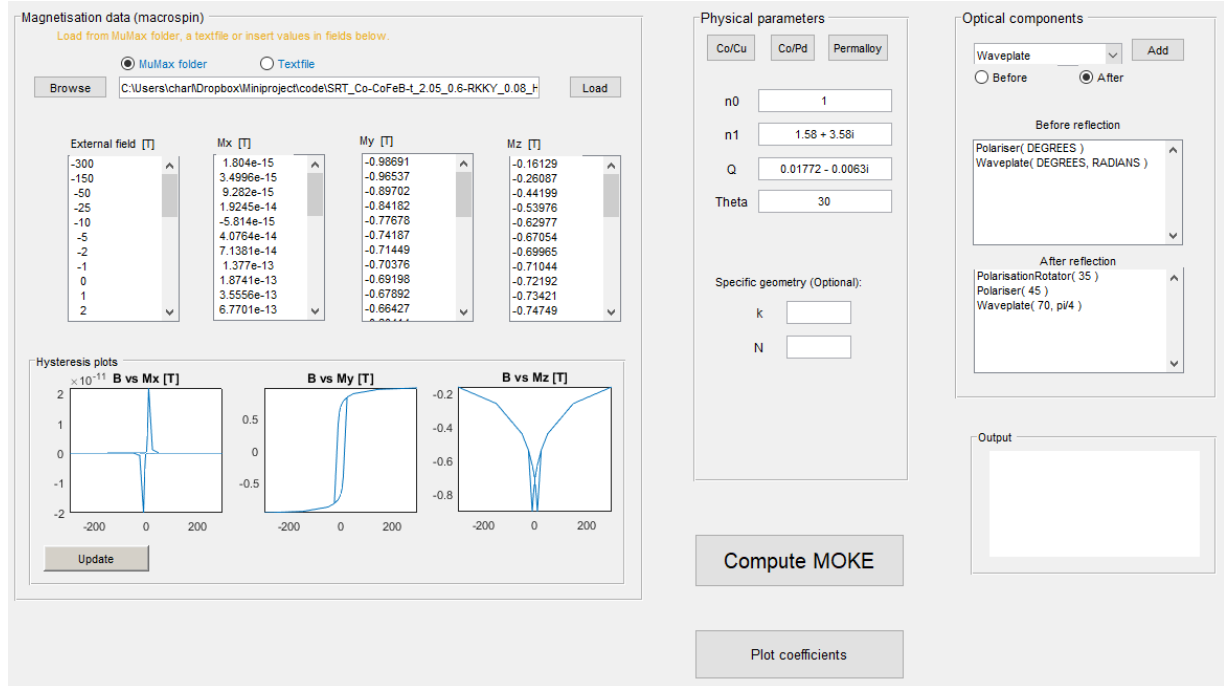


Figure 17: GUI to access the functionality of the developed API.

Optical components. To provide flexibility in having different means of preparation and detection of the incident and reflected polarisation state, respectively, the rubric to the right in the GUI allows for specifying various optical components before and/or after reflection. The components are those described in section 4, and their corresponding functions in the API can be selected with the dropdown menu in the top of the rubric. After selection the user can add the component by pressing the Add button, and depending on the toggles just below the dropdown menu, the component will be added to either the "Before reflection" or the "After reflection" textfield in the rubric. These textfields need to be manually edited to input arguments to the commands, which are either in units of degrees or radians. In the screenshot of figure 17 the "Before reflection" textfield show examples of commands whose argument has not yet been input, whereas the "After reflection" textfield show commands that have been edited. The only commands taking two arguments is the `Waveplate`, since one can both specify the angle of the fast axis relative to the p -axis (in degrees) and the birefringence (in radians).

Computation. After having considered all types of user input, the computation can be initiated with the Compute MOKE button, which spawns a new panel, which can be seen in appendix A. This new panel shows the predicted MOKE signal. The panel also features a slider that can be used to go through each calculated MOKE data point, which then updates three plots of polarisation in the panel. These three plots respectively

show the polarisation right before reflection (i.e. after the initial beam has passed through the "Before reflection" components but has not reached the sample yet), right after reflection (i.e. before the reflected beam passes through the "After reflection" components) and at the point of detection (i.e. after the reflected beam passes through the "After reflection" components).

Finally, in the main GUI pane the button "Plot coefficients", gives the option to spawn another pane for computing and visualising the real and imaginary parts of the MOKE Fresnel coefficients from section 2 based on the provided input. This pane is also shown in appendix A.

7 Outlook

There are several things that would be interesting to pursue as the next steps to take this project further. Some of them are:

- Use beam profile of the laser beam, e.g. a Gaussian beam, to compute a weighted magnetisation average.
- Account for penetration of the beam into the sample, i.e. perform the full volume integral. (28) rather than a surface integral, which would alter the effective magnetisation.
- Consider interferometric effects that may occur due to the penetration of the sample.
- Implement a scanning MOKE algorithm to systematically perform imaging and magnetic characterisation of a 3D object.

- Include noise sources to make computations more realistic and study robustness of the inverse problem methods in the presence of noise.
- Allow multiple separate structures to be present on the sample and consider the effect of occlusion and multiple reflections – essentially doing what is known as ray tracing in computer graphics.
- Evaluate the importance of quantum exchange interactions and whether it would be possible to extend the computations with a model for this.

Some work has been put into treating the beam profile, which will be elaborated briefly in the following. Furthermore, the next desired milestone, given a continuation of the project, which includes some of the points above will also be described.

Gaussian beam integration As was described in section 5, the MOKE computation performed so far have assumed that the spatial beam width of the laser in use is much larger than the length scale of the sample. If this was not the case, the effective magnetisation would have to be evaluated by the surface integral corresponding to (28) – under the assumption that the surface is perfectly reflective, otherwise it becomes a volume integral.

A Gaussian beam have several beam parameters: beam waist, depth of focus (or alternatively defined via the Rayleigh range) and beam divergence (angular spread) [12]. A thorough treatment of a Gaussian beam laser would incorporate all these parameters, but for now we shall assume that the Gaussian beam is collimated, which corresponds to the Rayleigh range being much larger than the propagation distance.

Given a Gaussian beam with a certain wave vector in space that is incident on the sample, the question is then how the Gaussian intensity distribution will look like on the surface of the sample. Let the sample be planar as before. It is clear that for oblique angles of incidence, the transformation of the Gaussian distribution should cause a distortion along the axes of the sample plane, which in general results in an asymmetric distribution. This projection of the distribution depends on the wave vector, \mathbf{k} , and the sample plane normal \mathbf{n} . If \mathbf{h} is a point in a cross-section of the beam somewhere in space before the incidence with the sample, a straight-forward projection onto the plane is given by

$$p_{\text{proj},\mathbf{n}}(\mathbf{h}) = \mathbf{h} - (\mathbf{h} \cdot \mathbf{n})\mathbf{n}, \quad (31)$$

assuming \mathbf{n} is normalised. Although this point lies in the sample plane, it is not in the correct position, because the corresponding ray in the beam would have propagated further along the direction of \mathbf{k} before being incident at the plane. Hence, it is necessary to project along the direction of \mathbf{k} , but replacing \mathbf{n} by \mathbf{k} in (31) does not produce a projected point, because the factor $\mathbf{h} \cdot \mathbf{k}$ would

not correspond to the correct distance between \mathbf{h} and the plane. The correct factor is found by extruding by an unknown amount from the point \mathbf{h} along \mathbf{n} onto the plane and solving for the distance, say x , i.e.

$$(\mathbf{h} + x\mathbf{k} - \mathbf{p}) \cdot \mathbf{n} = 0 \Leftrightarrow x = \frac{\mathbf{p} \cdot \mathbf{n} - \mathbf{h} \cdot \mathbf{n}}{\mathbf{k} \cdot \mathbf{n}}, \quad (32)$$

where \mathbf{p} is any point in the sample plane, because both a position and a normal is needed to uniquely define a plane in space.

The projection of the point \mathbf{h} is then given by

$$p_{\text{proj},\mathbf{k}}(\mathbf{h}) = \mathbf{h} + \frac{\mathbf{p} \cdot \mathbf{n} - \mathbf{h} \cdot \mathbf{n}}{\mathbf{k} \cdot \mathbf{n}} \mathbf{k}. \quad (33)$$

Apart from projecting the distribution, there is also an overall factor that is needed to scale the beam intensity at the sample plane. This factor is given by $|\mathbf{k} \cdot \mathbf{n}|$, and it can be derived by calculating how the length scales are projected via (33). Clearly, the intensity mapping is one-to-one, when the incidence is perpendicular as one would expect, and the more shallow the incidence, the more spread out the beam becomes, causing this factor to approach zero.

An example of this projection transformation in practice is shown on figure 18 for a system seen from two different directions. The height profiles of the Gaussian distributions have no geometrical significance; they are only included to emphasise the distortion of the distribution, since the colour coding is not very clear due to the beam being spread out on the projection plane.

After projection and scaling the surface integral can be evaluated numerically by a weighted double sum, akin

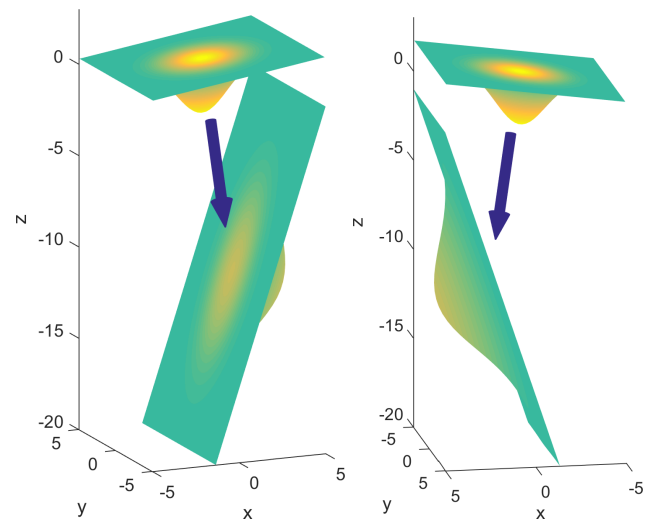


Figure 18: Example projection of a Gaussian beam profile onto an arbitrary planar sample in space. The parameters used are $\mathbf{n} = (1, 0, -7)$ (normalised), $\mathbf{k} = (-1, 0, 1/3)$ (normalised) and $\mathbf{p} = (5, 0, -1)$. The intensity scaling factor is $|\mathbf{k} \cdot \mathbf{n}| = 0.45$.

to (29), to find the effective magnetisation, where the weights are simply the projected Gaussian beam intensities at their corresponding positions in the sample plane.

Scanning MOKE After having fully implemented the Gaussian beam surface integration, and possibly the volume integration if material penetration is assumed, the next major milestone in a continuation of the project would be to implement a scanning algorithm to do imaging of the complete sample. The sample surface could be curved, in which case some 3D reconstructing would be required when using the technique of discretising a general 3D shape into planes as described in section (2.2). The sample could also be consisting of several smaller structures, for instance planes situated around a substrate like the experimentally realised scaffold in figure 2. In both cases a scanning of the complete sample would be necessary to fully characterise it, magnetically and geometrically.

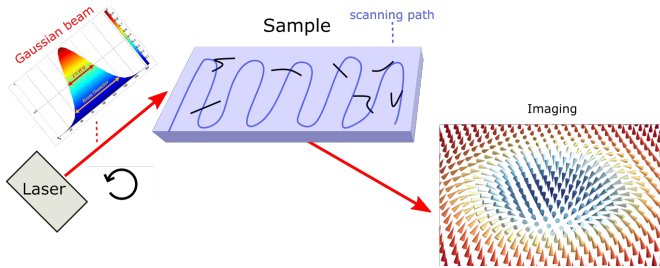


Figure 19: Next milestone in a continuation of the project. Beam profile is accounted for, and a scanning of the complete sample is done to finally produce an image of the geometry and magnetisation.

The envisioned implementation of this milestone is summarised by figure 19. In this implementation the Gaussian beam profile is taken into account, a path to sweep systematically sweep the sample is defined, and a subsequent reconstruction of the magnetic distribution and geometric layout is finally computed.

8 Conclusion

The theory behind oblique MOKE has been reviewed. An overview of some of the confusion in the literature has been obtained; not only of the different sign conventions and coordinate system definitions, but of several mistakes and typos that in one case survived through papers from multiple authors.

The theory has been further extended to a 3D setting, such that computations can be done for generalised configurations in 3D space. This 3D extension formed the foundation in which the so-called inverse problems could be treated, namely the problems of inferring both the sample's geometry and magnetisation only by probing it with beams from a distance. The inverse geometry problem was found to be solvable with two beams that have

slightly different initial positions or initial wave vectors assuming that the reflected beams can be located. This procedure leads to a system of 10 nonlinear equations and 9 unknowns, and a numerical method to solve it has been proposed. The inverse magnetisation problem was found to be solvable with two beams that have different initial polarisation states, but also requires the geometry to be known, and so a succession of the schemes would be required, in which case a total of three beams would suffice, since one of the two beams used for the inverse geometry problem can be reused. The scheme for the inverse magnetisation problem leads to a system of 6 nonlinear equations and 5 unknowns, and again a numerical method has been proposed.

The numerical method of choice is a nonlinear least squares method based on a trust region algorithm, which is able to handle parameter bounds contrary to the common Newton step-based Levenberg-Marquardt algorithm. The numerical method has been demonstrated to be consistent, i.e. exhibits convergence when numerical stability is assumed, for a vast number of random starting guesses within the bounds. A significant performance gap was found between the two inverse problems' methods, and the difference has been ascribed to how well each objective function is approximated by a linearisation.

Using MOKE for characterising hysteresis in simulations has been covered, and predictions given a specific distribution of magnetisation have been computed and compared to experimentally obtained measurements. The beam profile and material penetration was neglected, which is only a valid approximation if the beam width is much larger than the length scale of the sample, or if the magnetisation is relatively uniform throughout the sample. The magnetisation data used to represent the sample of the experiment was obtained from the simulation software MuMax, provided by supervisor. The magnetisation according to this simulation was indeed found to be relatively uniform, and so the approximations may not be so crude. The predictions also turned out to agree reasonably well with the experimental measurements. Important features occurred in both the numerical and experimental signals; the general symmetry of the ellipticity measurement was consistent, and a certain asymmetry in the rotation measurement was also observed in both. However, a non-reproducible bias was found for both measurements, which is expected to be a well-known phenomenon called exchange bias caused by noncollinear quantum exchange interaction.

Some of the implementations developed during this project have been put into an API and a GUI has been designed as a front-end. It is the hope that this tool for generalised 3D MOKE computations and hysteresis simulations may be of use to researchers in the field. The tool has been briefly documented in the report.

There are many next steps that could be taken in a continuation of the project, some of which have been de-

scribed. Firstly, it would be worthwhile to consider computations that account for beam profiles. Some effort has been put into treating a Gaussian beam profile in a 3D setting. The transformation of a Gaussian beam intensity distribution onto an oblique plane has been derived, which makes it possible to find the effective magnetisation with a weighted surface integral. However, while the transformation and integration have been done, no MOKE computations with Gaussian beams have been done, and one of the next objectives would be to do just that. The next major milestone would be to have a scanning algorithm to perform imaging and magnetic characterisation of a complete sample possibly with a non-planar geometry and assuming a Gaussian beam.

References

- [1] Jeffrey McCord. Progress in magnetic domain observation by advanced magneto-optical microscopy. *Journal of Physics D: Applied Physics*, 48(33):333001, August 2015.
- [2] JP Jamet, J Ferré, P Meyer, J Gierak, C Vieu, F Rousseaux, C Chappert, and V Mathet. Giant enhancement of the domain wall velocity in irradiated ultrathin magnetic nanowires. *IEEE transactions on magnetics*, 37(4):2120–2122, 2001.
- [3] Mark R Freeman and Wayne K Hiebert. Stroboscopic microscopy of magnetic dynamics. In *Spin Dynamics in Confined Magnetic Structures I*, pages 93–126. Springer, 2002.
- [4] Alex Hubert and Rudolf Schäfer. Magnetic domains: The analysis of magnetic microstructure. *Magnetic domains: the analysis of magnetic microstructure*, 1998.
- [5] Amalio Fernández-Pacheco, Robert Streubel, Olivier Fruchart, Riccardo Hertel, Peter Fischer, and Russell P. Cowburn. Three-dimensional nanomagnetism. *Nature Communications*, 8:15756, June 2017.
- [6] Robert Streubel, Peter Fischer, Florian Kronast, Volodymyr P. Kravchuk, Denis D. Sheka, Yuri Gaididei, Oliver G. Schmidt, and Denys Makarov. Magnetism in curved geometries. *Journal of Physics D: Applied Physics*, 49(36):363001, 2016.
- [7] Dan A Allwood, Gang Xiong, CC Faulkner, D Atkinson, D Petit, and RP Cowburn. Magnetic domain-wall logic. *Science*, 309(5741):1688–1692, 2005.
- [8] JA Currivan-Incorvia, S Siddiqui, S Dutta, ER Evarts, J Zhang, D Bono, CA Ross, and MA Baldo. Logic circuit prototypes for three-terminal magnetic tunnel junctions with mobile domain walls. *Nature communications*, 7:10275, 2016.
- [9] Jacob Torrejon, Mathieu Riou, Flavio Abreu Araujo, Sumito Tsunegi, Guru Khalsa, Damien Querlioz, Paolo Bortolotti, Vincent Cros, Akio Fukushima, Hitoshi Kubota, and others. Neuromorphic computing with nanoscale spintronic oscillators. *arXiv preprint arXiv:1701.07715*, 2017.
- [10] Dédalo Sanz-Hernández, Ruben F. Hamans, Jung-Wei Liao, Alexander Welbourne, Reinoud Lavrijsen, and Amalio Fernández-Pacheco. Fabrication, Detection, and Operation of a Three-Dimensional Nanomagnetic Conduit. *ACS Nano*, 11(11):11066–11073, November 2017.
- [11] D. A. Allwood, Gang Xiong, M. D. Cooke, and R. P. Cowburn. Magneto-optical Kerr effect analysis of magnetic nanostructures. *Journal of Physics D: Applied Physics*, 36(18):2175, 2003.
- [12] Bahaa EA Saleh, Malvin Carl Teich, and Bahaa E Saleh. *Fundamentals of Photonics*, volume 22. Wiley New York, 1991.
- [13] Ml Freiser. A survey of magneto-optic effects. *IEEE Transactions on magnetics*, 4(2):152–161, 1968.
- [14] G. P. Agrawal. *Nonlinear Fiber Optics*. Elsevier/Academic Press, Amsterdam, fifth edition edition, 2013.
- [15] Robert W Boyd. *Nonlinear Optics*. Academic press, 2003.
- [16] Chun-Yeol You and Sung-Chul Shin. Derivation of simplified analytic formulae for magneto-optical Kerr effects. *Applied Physics Letters*, 69(9):1315–1317, August 1996.
- [17] Chun-Yeol You and Sung-Chul Shin. Generalized analytic formulae for magneto-optical Kerr effects. *Journal of Applied Physics*, 84(1):541–546, July 1998.
- [18] Robert P. Hunt. Magneto-Optic Scattering from Thin Solid Films. *Journal of Applied Physics*, 38(4):1652–1671, March 1967.
- [19] Z. J. Yang and M. R. Scheinfein. Combined three-axis surface magneto-optical Kerr effects in the study of surface and ultrathin-film magnetism. *Journal of Applied Physics*, 74(11):6810–6823, December 1993.
- [20] Vladimir Protopopov. *Practical Opto-Electronics*. Springer, 2014.
- [21] T. H. J. Loughran, P. S. Keatley, E. Hendry, W. L. Barnes, and R. J. Hicken. Enhancing the magneto-optical Kerr effect through the use of a plasmonic antenna. *Optics Express*, 26(4):4738, February 2018.

- [22] Stephen Wright and Jorge Nocedal. Numerical optimization. *Springer Science*, 35(67-68):7, 1999.
- [23] Randall J LeVeque. Finite difference methods for differential equations. *Draft version for use in AMath*, 585(6), 1998.
- [24] José J Gil and Eusebio Bernabeu. Obtainment of the polarizing and retardation parameters of a non-depolarizing optical system from the polar decomposition of its Mueller matrix. *Optik*, 76(2):67–71, 1987.
- [25] P Monod, JJ Prejean, and B Tissier. Magnetic hysteresis of CuMn in the spin glass state. *Journal of Applied Physics*, 50(B11):7324–7329, 1979.
- [26] Arne Vansteenkiste and Ben Van de Wiele. Mumax: A new high-performance micromagnetic simulation tool. *Journal of Magnetism and Magnetic Materials*, 323(21):2585–2591, 2011.
- [27] Mark Fox. *Optical Properties of Solids*, volume 3. Oxford university press, 2010.
- [28] FC Ummelen, Amalio Fernández-Pacheco, Rhodri Mansell, DCMC Petit, HJM Swagten, and Russell Paul Cowburn. Controlling the canted state in antiferromagnetically coupled magnetic bilayers close to the spin reorientation transition. *Applied Physics Letters*, 110(10):102405, 2017.
- [29] Elena Y Vedmedenko, Jon A Arregi, Patricia Riego, and Andreas Berger. Interlayer Dzyaloshinskii-Moriya interactions. *arXiv preprint arXiv:1803.10570*, 2018.
- [30] Oscar Ávalos-Ovando, Diego Mastrogiuseppe, and Sergio E Ulloa. Noncollinear exchange interaction in transition metal dichalcogenide edges. *Physical Review B*, 93(16):161404, 2016.
- [31] Shuai Dong, Kunihiko Yamauchi, Seiji Yunoki, Rong Yu, Shuhua Liang, Adriana Moreo, J-M Liu, Silvia Picozzi, and Elbio Dagotto. Exchange bias driven by the Dzyaloshinskii-Moriya interaction and ferroelectric polarization at G-type antiferromagnetic perovskite interfaces. *Physical review letters*, 103(12):127201, 2009.

Appendices

A Assisting GUI panes

Figure 20 shows two panes that are brought forth by pressing the "Compute MOKE" or "Plot coefficients" buttons, respectively, in the main interface.

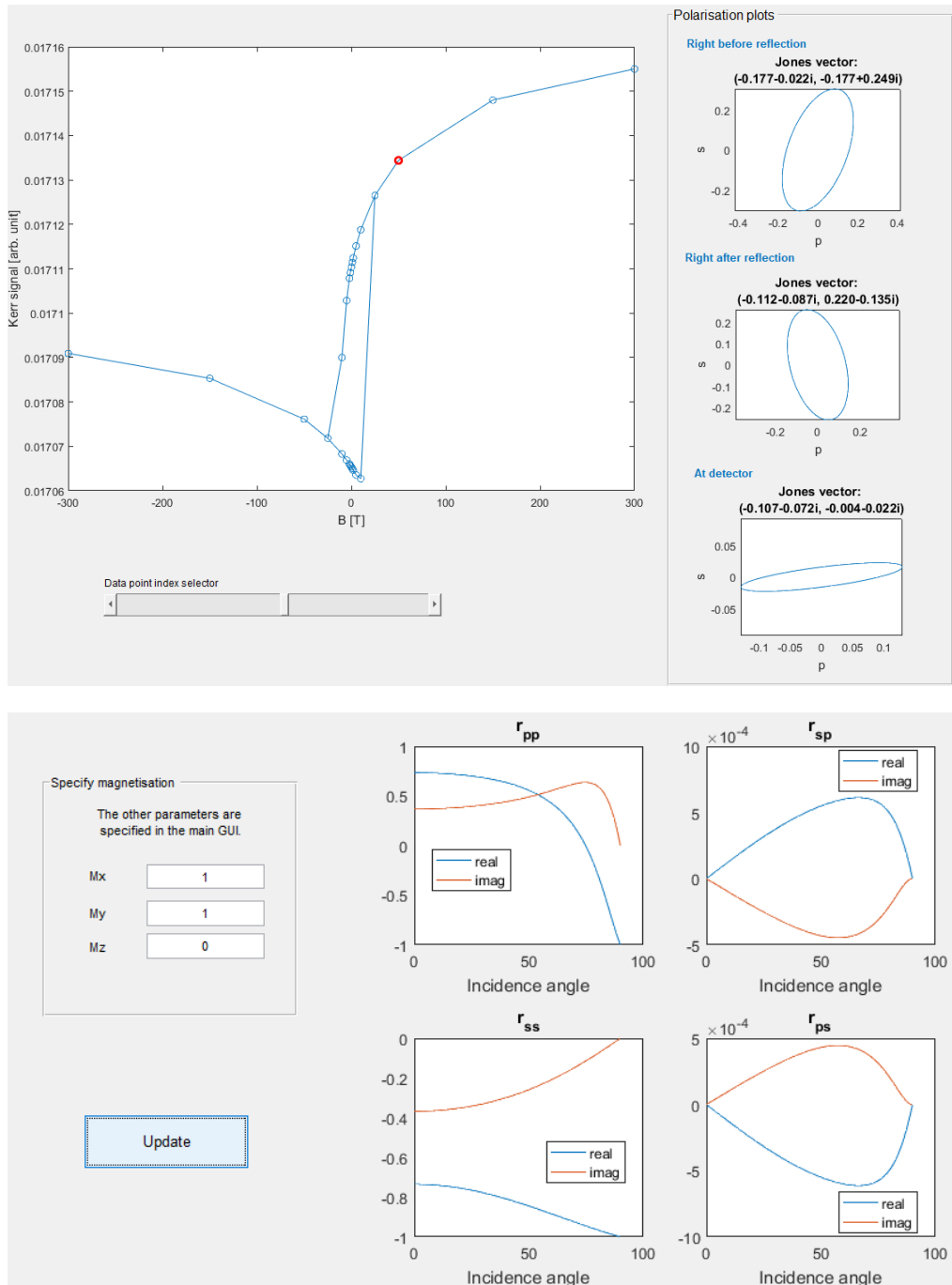


Figure 20: (Upper GUI pane) Visualisation of a MOKE signal hysteresis loop with a slider to go through each calculated MOKE data point (current selection indicated by the red circle in the main plot), which updates the three polarisation plots in the right. (Lower GUI pane) Plots of the MOKE coefficients based on a specified magnetisation vector (components M_x , M_y , M_z) and the other physical parameters provided in the main GUI pane.